Red blood cell dynamics in extravascular biological tissues modelled as canonical disordered porous media

Qi Zhou[1,*], Kerstin Schirrmann[2,3], Eleanor Doman[4], Qi Chen[2,3], Naval Singh[2,3], P. Ravi Selvaganapathy[5], Miguel O. Bernabeu[6,7], Oliver E. Jensen[4], Anne Juel[2,3], Igor L. Chernyavsky[4,8], and Timm Krüger[1,*]

[1]School of Engineering, Institute for Multiscale Thermofluids, University of Edinburgh, UK
[2]Manchester Centre for Nonlinear Dynamics, University of Manchester, UK
[3]Department of Physics and Astronomy, University of Manchester, UK
[4]Department of Mathematics, University of Manchester, UK
[5]Department of Mechanical Engineering, School of Biomedical Engineering, McMaster University, Canada
[6]Centre for Medical Informatics, Usher Institute, University of Edinburgh, UK
[7]Bayes Centre, University of Edinburgh, UK
[8]Maternal and Fetal Health Research Centre, School of Medical Sciences, University of Manchester, UK
[*]Corresponding authors: q.zhou@ed.ac.uk (Q.Z.); timm.krueger@ed.ac.uk (T.K.)

Abstract

The dynamics of blood flow in the smallest vessels and passages of the human body, where the cellular character of blood becomes prominent, plays a dominant role in the transport and exchange of solutes. Recent studies have revealed that the micro-haemodynamics of a vascular network is underpinned by its interconnected structure, and certain structural alterations such as capillary dilation and blockage can substantially change blood flow patterns. However, for extravascular media with disordered microstructure (e.g., the porous intervillous space in the placenta), it remains unclear how the medium's structure affects the haemodynamics. Here, we simulate cellular blood flow in simple models of canonical porous media representative of extravascular biological tissue, with corroborative microfluidic experiments performed for validation purposes. For the media considered here, we observe three main effects: first, the relative apparent viscosity of blood increases with the structural disorder of the medium; second, the presence of red blood cells (RBCs) dynamically alters the flow distribution in the medium; third, increased structural disorder of the medium can promote a more homogeneous distribution of RBCs. Our findings contribute to a better understanding of the cell-scale haemodynamics that mediates the relationship linking the function of certain biological tissues to their microstructure.

Keywords: Haemodynamics, Red blood cells, Biological tissues, Porous media, Lattice-Boltzmann, Microfluidics

1 Introduction

Significant progress in computational modelling has been made over recent years to elucidate the complex behaviour of blood flow in physiological environments, *e.g.*, the small-vessel network in the brain [1, 2, 3], in the eye [4, 5], in tumours [6], and in microaneurysms [7]. However, the flow and transport of blood and solutes in other (*e.g.*, extravascular) types of biological media with vital function, such as the intervillous space (IVS) of the human placenta featuring a highly disordered network of pores and flow passages of size comparable to that of red blood cells (RBCs), remain poorly understood [8, 9].

Comprehensive theories of flow and transport in porous media have been established, revealing subtle relationships between pore-scale structural heterogeneity and macroscopic flow properties [10, 11, 12,

13]. However, existing models of flow through porous media often assume a homogeneous fluid and cannot accurately infer the intricate blood rheology in living biological media, such as the IVS, where the particulate and highly-confined character of blood plays a key role, introducing spatiotemporal variability and nonlinearity beyond the description of prevalent continuum models [14, 15].

Emerging cell-resolved models of blood flow using advanced mesoscopic methods [16, 17, 18, 19] have been extensively applied since the late 2010s to simulate multiscale haemodynamics in synthetic or realistic vascular networks. These simulations have greatly improved our understanding of microscopic processes in the blood stream mediated by the flowing RBCs within, *e.g.*, biased haematocrit distribution and oxygen transport arising from abnormal branching patterns of the vasculature [20].

Facilitated by robust image segmentation and meshing techniques [21, 22], cell-resolved models are now technically applicable to living porous media. These models provide a promising avenue for microscopic characterisation of the microstructure-dependent cellular blood flow, which can inform generalised constitutive relationships. A key aim is the development of effective reduced-order models for simulating large tissue/organ systems [23]. Additionally, cellular simulations can help design and optimise microfluidic oxygenators that serve as artificial lung assist devices [24].

In this work, we aim to characterise microscopic blood flow in canonical porous medium models constructed to represent simplistic extravascular biological media, for which we have control over the structural characteristics that can be related to physiological or pathological conditions of porous tissues and organs. Specifically, our focus is to quantify the correlations between cell-scale haemodynamics (*e.g.*, flow patterns, RBC partitioning, haematocrit distribution) and key metrics of the porous medium, such as porosity and disorder. Primarily, we tackle the task computationally, with the aid of microfluidic experiments in equivalent flow systems for validation.

2 Methods

2.1 Design of canonical disordered porous media

We consider two typical designs of planar (quasi-2D) canonical disordered porous media (DPM) for our 3D simulations and validating experiments: *locally perturbed media (LPM)* (Fig. 1A) representing weak-disorder systems and *globally random media (GRM)* (Fig. 1C) representing strong-disorder systems, both of which are in the form of non-overlapping uniformly sized cylinders. The design process is inspired by the "bundle of tubes (uniform)" model implemented by Gostick *et al.* [25].

To obtain LPM, we first construct an ordered porous medium (OPM) by placing cylinders of constant diameter D_c (determined by porosity ϕ and domain size) on a square grid with length L and width W (Fig. 1A inset), which can be regarded as a generalised capillary bundle model. Three porosity values $\phi = 0.57, 0.62, 0.67$ are considered, which lead to a confinement ratio (defined as $\chi = D_{\mathrm{RBC}}/W_{\mathrm{throat}}$, denoting the ratio of effective RBC diameter to throat width) in the baseline OPM geometry of $\chi = 1.2, 1.0, 0.9$, respectively. The alteration of porosity is achieved by varying D_c while keeping the cylinder positions unchanged. The structural disorder of the LPM is then created by introducing random perturbations to the cylinder positions (x, y) with standard deviation $\sigma = 0.1, 0.3, 0.5, 0.7$, where (x, y) are drawn from a bivariate normal distribution. For a relatively large σ (*e.g.*, $\sigma = 0.7$), the perturbations are likely to cause overlapping cylinders and several attempts may be needed to construct a non-overlapping layout. The resulting distributions of throat widths in the LPM are Gaussian (Fig. 1B).

The GRM is constructed by placing a uniformly random spatial distribution of cylinders in a domain of given size for a designated porosity ($\phi = 0.66$), while enforcing a minimal separation distance of $0.4D_{\mathrm{RBC}}$ between neighbouring cylinders (Fig 1C). The resulting distribution of throat widths in the GRM is approximately exponential (Fig 1D).

For ease of description when comparing various geometries in plots, each LPM geometry is assigned with a disorder identifier and a porosity identifier, *e.g.*, LPM-σ0.5-ϕ0.57 for LPM with $\sigma = 0.5$, $\phi = 0.57$.
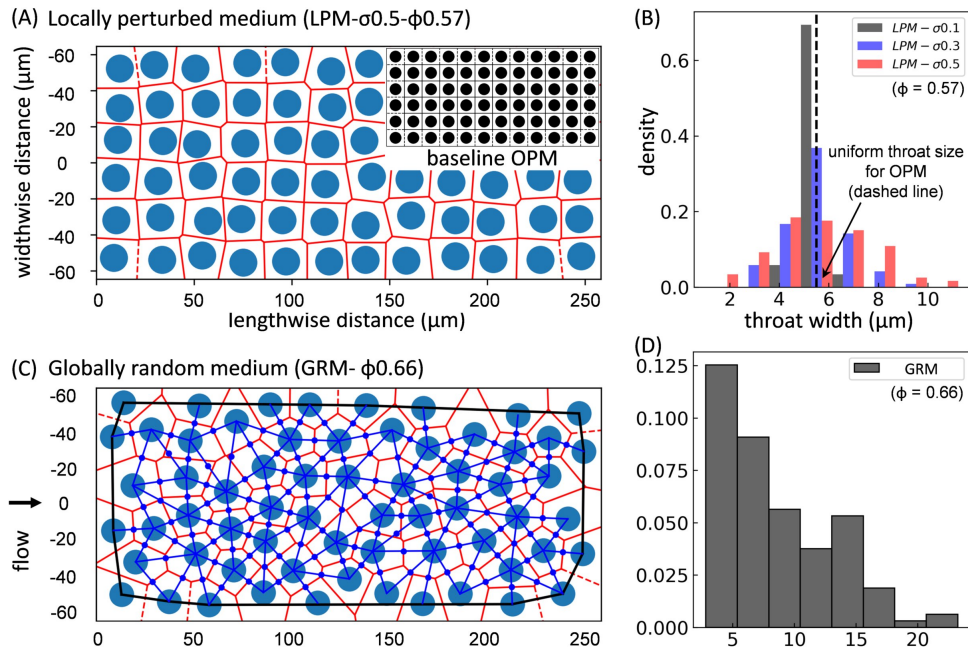
Figure 1: **Construction of canonical porous media.** (A) Locally perturbed medium (LPM), constructed by introducing local perturbations to a periodic ordered medium (OPM) of square obstacle arrays (inset). The throats (red edges) are delineated by Voronoi tessellation (red polygons); the pores are located where neighbouring edges meet. (B) Throat-width distributions (in the form of normalised histograms) for LPM geometries perturbed from an OPM of porosity $\phi = 0.57$, with incremental disorder $\sigma = 0.1, 0.3, 0.5$. (C) Globally random medium (GRM) with pores and throats (excluding those in direct contact with the boundaries, which are located outside the black bounding box) delineated by Voronoi tessellation (red polygons) and Delaunay triangulation (blue triangles). The blue dots indicate the middle points of pore openings where local flows and cell fluxes are evaluated. (D) Throat-width distribution for GRM ($\phi = 0.66$), same axis labels as (B). Flow is driven in the horizontal direction.

For OPM and GRM, only a porosity identifier is assigned, *e.g.*, OPM-$\phi0.57$ and GRM-$\phi0.66$.

2.2 Numerical model

The immersed-boundary-lattice-Boltzmann method (IB-LBM [26]) simulates cellular blood flow as a suspension of deformable RBCs (see Sec. S1 in the **Supplementary Material** for more details of the model) through a shallow Hele-Shaw bed ($L \times W \times H = 258 \times 129 \times 6 \ \mu m^3$) of vertical cylinders, which is constructed through extrusion over a distance (H) of the desired DPM designs of dimension $L \times W$ (LPM or GRM) in the depth direction. Each RBC is modelled through the finite element method as a closed hyperelastic membrane with the unstressed shape of a biconcave discoid. The mechanical properties of the RBC membrane are controlled by elastic moduli accounting for different energy contributions, including the strain modulus κ_s, bending modulus κ_b, dilation modulus κ_α, surface modulus κ_A and volume modulus κ_V [27] (see Table S1). To tackle close cell-cell and cell-wall interactions, a repulsion potential decaying with inverse distance between neighbouring surfaces is numerically implemented with interaction intensities comparable to the bending elasticity of the RBC membrane [28].

In the simulations, an RBC-free plasma flow is initialised from left to right along the channel axis (length direction) with a designated volumetric flow rate Q_0 (Fig. 2A). The flow is driven by imposing a
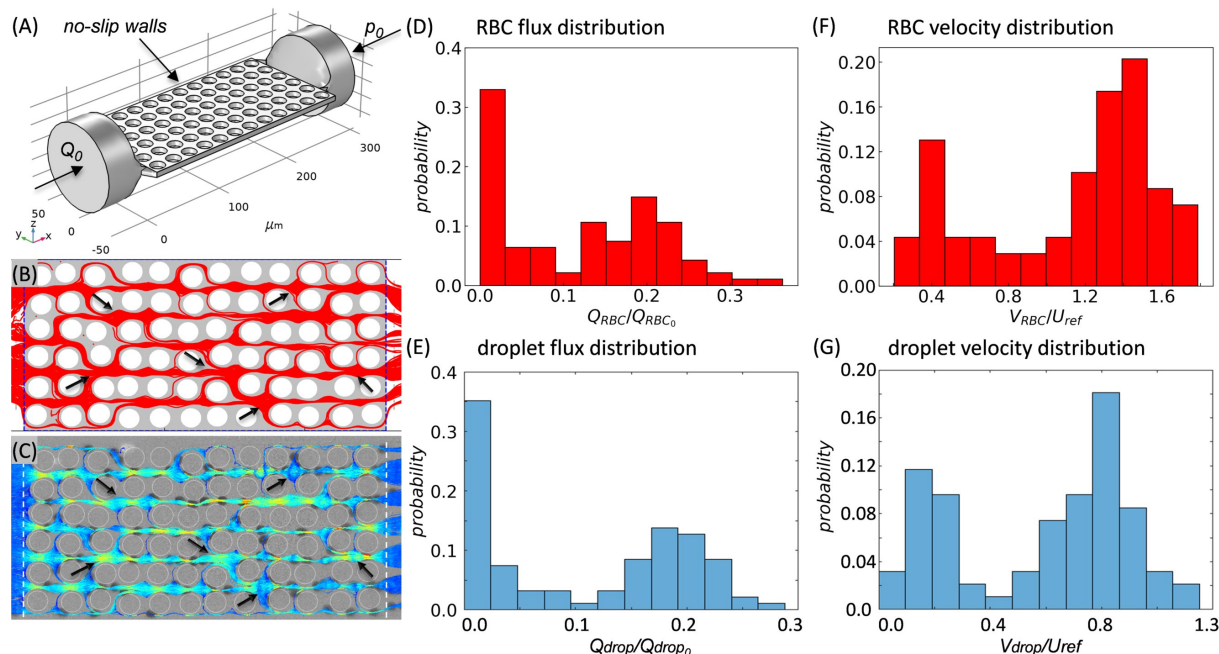
3

Figure 2: **Cross-validation of simulation and experiment (LPM-σ0.5-ϕ0.57).** (A) Schematic of simulation domain and boundary conditions. (B,D,F) Simulation results. (C,E,G) Experiment results. (B,C) Superimposed particle trajectories over time. The red lines in (B) represent the RBC trajectories, and the red dots indicate occluded throats by the RBCs. The coloured lines in (C) represent the droplet trajectories with high-velocities marked in brighter colours. The black arrows in (B,C) highlight example regions of interest where simulation and experiment agree well. (D,E) Distributions of normalised particle fluxes. (F,G) Distributions of normalised particle speed.

parabolic velocity profile at the inlet (assuming Poiseuille flow under Q_0) and a reference pressure at the outlet (p_0), through two cylindrical flow extensions smoothly stitched to the porous bed of rectangular cross-section $(W \times H)$. The no-slip condition is imposed at the wall and all fluid-solid interfaces. Once the plasma flow is converged, RBCs are randomly inserted from the inlet flow extension in a continuous manner with fixed RBC volume fraction (*i.e.*, feeding discharge haematocrit, $H_\mathrm{F} = 0.1, 0.2, 0.3$). RBCs reaching the outlet flow extension are removed from the system (see **Supplementary Movie1** for an example simulation in the OPM-ϕ0.57 geometry).

2.3 Microfluidic experiments

In the microfluidic experiments, a suspension of silicone oil droplets (Sigma Aldrich, viscosity $\nu = 20$ cSt with paraffin oil dye) in a mixture of water and glycerol (Sigma Aldrich, 80:20 by volume with 0.2% SDS, viscosity 0.24 Pa s at 21°C) is used as biomimetic model for blood. The droplets were generated in a flow-focusing device [29] which was connected to the porous medium via a bent glass capillary (length 100 mm, outer diameter 1 mm, inner diameter 0.58 mm). Droplets with a diameter of $240\,\mu$m were produced by flowing the inner phase (silicone oil) at $4\,\mu$L/min and introducing the outer phase (water/glycerol) through a cross-junction at $5\,\mu$L/min immediately upstream of the flow-focusing channel constriction. Downstream of the droplet formation, another 11 μl/min of water-glycerol mix was added to set the droplet flow fraction to $H_\mathrm{F} = 0.2$. Flow control at the different inlets was achieved with a combination of

4

a pressure controller (Elvesys) fitted with flow meters and a syringe pump (KD Scientific). Both the flow-focusing device and the porous medium were made from PDMS (Polydimethylsiloxane, Sylgard 184, Dow Corning). To obtain hydrophilic wetting behaviour, the devices were oxidised by oxygen plasma treatment (Henniker plasma HPT-100) and immediately filled with water. The porous medium corresponds to the LPM-$\sigma 0.5$-$\phi 0.57$ geometry (*i.e.*, disorder 0.5 and porosity 0.57) used in numerical simulations, scaled by the ratio of the droplet diameter to the equivalent diameter of simulated RBCs ($D_{\text{RBC}} = 6.68 \ \mu$m). The suspension flow was imaged with a monochrome CMOS camera (PCO 1200hs) and analysed off-line using the ImageJ platform TrackMate [30].

2.4 Cross-validation of simulation and experiment

Good agreement between the simulated and experimented particle dynamics is obtained (see Fig. 2B–G and **Supplementary Movie2–Movie3** for comparison in an example geometry), including the pattern of particle trajectories (Fig. 2B,C), the distribution of particle fluxes (Fig. 2D,E) and the distribution of particle velocities (time-average speed for particles crossing a given pore-throat, Fig. 2F,G). Both the RBCs and droplets demonstrate evident preferential pathways or regional shunts when travelling across the porous domain, with discrete clusters of high-flux and low-flux throats. Similarly, the mean particle velocities at individual throats feature a bimodal distribution where high-velocity and low-velocity populations co-exist.

Here, particle fluxes Q_{RBC} (or Q_{drop}) and particle speed V_{RBC} (or V_{drop}) are evaluated at individual throats in the porous domain. Taking the simulation for example, Q_{RBC} is defined as

$$Q_{\text{RBC}} = Q_{\text{blood}} H_{\text{d}}, \tag{1}$$

where Q_{blood} is the local volumetric flow rate (denoted as Q_{p} in plasma flow and Q_{s} in suspension flow) across a given throat and H_{d} is the discharge haematocrit measured for the same throat. The normalising particle flux Q_{RBC0} is chosen as the overall particle flux fed at the flow inlet; it is defined as

$$Q_{\text{RBC0}} = Q_0 H_{\text{F}}, \tag{2}$$

where Q_0 is the flow rate imposed at the inlet. The normalising particle velocity U_{ref} is chosen as the peak fluid velocity evaluated at the centre of horizontal pores in the baseline OPM geometry, defined as

$$U_{\text{ref}} = Q_{\text{throat}}/W_{\text{throat}} H, \quad Q_{\text{throat}} = Q_0/N, \tag{3}$$

where the throat width W_{throat} measures the minimum distance between two neighbouring cylinders and N is the number of throats across the vertical direction (perpendicular to flow axis) in the OPM geometry. Note that U_{ref} should not be mistaken for U_0, which is the superficial velocity U_0 defined as

$$U_0 = Q_0/WH. \tag{4}$$

U_0 is adopted as spatially averaged advection speed to estimate the reference transit time T_{ref} for particles to travel across the whole domain length, defined as

$$T_{\text{ref}} = L/U_0. \tag{5}$$

3 Results and Discussion

We first demonstrate the effect of porous medium structure and the presence of RBCs on the flow resistance. Then, we investigate the RBCs' contribution to pore-scale flow redistribution and the RBCs' spatiotemporal dynamics in relation to structural characteristics of the porous domain.

3.1 Effect of structural disorder on flow resistance in porous media is more prominent with RBCs present
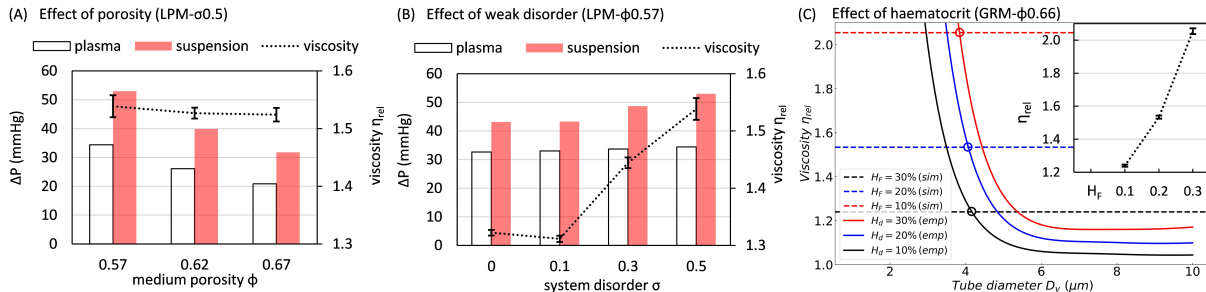

Figure 3: **Evaluation of flow resistance in porous media with different geometries and flow conditions.** Pressure drop across the simulated porous media under designated volumetric flow rates Q_0 fed at the inlet ($Q_0 = 0.4\,\mu\text{L/min}$ unless specified otherwise). The default porosity is $\phi = 0.57$. (A) Variation of pressure drop against porosity in LPMs of fixed disorder $\sigma = 0.5$ for plasma flow and a suspension flow with RBCs of feeding haematocrit $H_F = 0.2$. The relative apparent viscosity η_{rel} of the suspension flowing within is assessed through comparing with plasma viscosity. The error bars represent standard deviation of measurements from five time instants of the suspension flow. (B) Variation of pressure drop against disorder ($\sigma = 0.1, 0.3, 0.5$) in LPMs of fixed porosity $\phi = 0.57$ for plasma flow and a suspension flow with $H_F = 0.2$, where η_{rel} is quantified the same way as in (A). (C) Comparison of η_{rel} (dashed horizontal lines) in the simulated porous media with empirical predictions (solid curved lines) for straight tubes *in vitro* [31]. The round symbols indicate the characteristic diameter D_v of an equivalent tube within which the suspension has the same relative apparent viscosity. The inset of (C) shows the variation of simulated η_{rel} against increasing $H_F = 0.1, 0.2, 0.3$ in the GRM ($\phi = 0.66$).

To assess the resistance to plasma flow (RBC-free) and suspension flow (RBC-laden, with default feeding haematocrit $H_F = 0.2$), we compare the overall pressure drop ΔP across different porous media under an identical feeding volumetric flow rate at the inlet ($Q_0 = 0.4\ \mu\text{L/min}$ in simulations, unless otherwise specified). For suspension flow, we also examine the relative apparent viscosity η_{rel} comparing the suspension apparent viscosity η_{app} to that of plasma η_0 (1×10^{-3} Pa s), which can be calculated as the ratio of pressure drops for equivalent suspension and plasma flows under same inflow ($Q_s = Q_p = Q_0$), *i.e.*, $\eta_{\text{rel}} = \eta_{\text{app}}/\eta_0 = \Delta P_s/\Delta P_p$.

The porosity is found to have a prominent effect on the plasma flow resistance (Fig. 3A). For instance, a decrease of $\phi = 0.67$ to 0.62 and 0.57 for the intermediately disordered LPM ($\sigma = 0.5$) leads to 25.4% and 65.1% rise in the pressure drop, respectively. Similarly, the suspension also experiences higher flow resistance: 25.6% and 66.7% increase, respectively (Fig. 3A). However, the relative apparent viscosity of the suspension remains approximately constant, therefore suggesting a small effect of porosity within the studied range (Fig. 3A).

For a given porosity of $\phi = 0.57$, our simulations in LPM geometries reveal a marginal effect of incremental disorder on the resistance of plasma flow, but an evident effect on that of the suspension flow (Fig. 3B). The relative apparent viscosity increases substantially beyond a critical degree of disorder; η_{rel} is 16.4% higher at $\sigma = 0.5$ compared to its value in the ordered medium ($\sigma = 0$).

We further investigate the effect of stronger disorder on the relative apparent viscosity of suspension flow with the GRM geometry where random disorder is introduced globally (Fig. 3C). Different haematocrit levels are examined, with the RBC volume fraction varying between $H_F = 0.1 - 0.3$, which brings up the relative apparent viscosity by nearly 66%. The viscosity values ($\eta_{\text{rel}} \in [1.24, 2.05]$) are in line with recent experimental results for a large-scale porous domain consisting of hexagonal arrays of circular

pillars separated by a constant distance of 10 μm [32]. In our case, this distance is represented by the throat width W_{throat}. For the GRM geometry W_{throat} is not constant, but rather has an exponential distribution with a mean value of 8.5 μm and a median of 7.1 μm ($W_{\text{throat}} \in [2.8, 23.3]$ μm). Through comparison with an established empirical model for blood viscosity *in vitro* [31] (see the formulation in Sec. S2 of the **Supplementary Material**), our simulated suspension flow at $H_{\text{F}} = 0.1$, 0.2, 0.3 through the GRM domain is found to have equivalent relative apparent viscosity to a uniform cylindrical tube of 4.2 μm, 4.1 μm, 3.8 μm, respectively (Fig. 3C).

The significantly different effects of porosity and disorder on the relative apparent viscosity is surprising; both decreasing ϕ and increasing σ are expected to contribute to stronger pore-scale confinement that impedes the transport of RBCs [33] (see definition of confinement ratio χ in Sec. 2.1). We believe this difference in behaviour stems from the sensitivity of local confinement to changes in ϕ and σ. Changing ϕ uniformly modifies all throats (for $\phi \in [0.57, 0.67]$, the mean throat width only varies in the range of $\overline{W}_{\text{throat}} \in [5.5, 7.5]$ μm). In contrast, a change in σ augments the possibility of severe confinement in the system by broadening the W_{throat} distribution and giving rise to exceedingly small throats ($W_{\text{throat}} < 3\,\mu$m, see Fig. 1B). Note, however, that the impact of occasional severe confinement in some throats when increasing σ might be partially compensated by the simultaneously introduced larger throats, leading to an overall minor increment in the relative apparent viscosity.

Theoretically, when the size of a channel approaches that of an RBC, the cell-free layer vanishes due to confinement and the cells are in direct contact with the wall, consequently increasing the relative apparent viscosity of blood in straight tubes as postulated by the well-known Fåhræus-Lindqvist effect [31] (Fig. 3C). However, depending on its severity, such confinement may also contribute to lower relative apparent viscosity by forcing the organisation of RBCs into streamlined single-file form, thus excluding excessive cell-cell collisions that would otherwise increase flow resistance [14]. For the disordered geometries studied here, where a tightly interconnected network of pores and throats (rather than isolated channels) are involved, it is expected that both effects exist and compete with each other in determining the relative apparent viscosity of the suspension flow. Further, because each throat has a varying cross-section of contraction and expansion, the spatial organisation of RBCs constantly re-arranges without reaching a fully developed profile, which constitutes a mechanism for higher relative apparent viscosity in the porous medium than straight tubes of geometrically equivalent diameter (Fig. 3C). These counteracting mechanisms associated with structural alterations sometimes balance each other and the overall viscosity of the suspension remains roughly unchanged under certain circumstances (*e.g.*, Fig. 3A).

3.2 RBC traffic dynamically alters the pore-scale flow distribution

For both the plasma flow and suspension flow (Fig. 4A), a larger degree of structural disorder (*i.e.*, increasing σ) is found to promote higher perfusion of the pore space network as indicated by a smaller percentage of throats experiencing negligible flux (compare Fig. 4B with Fig. S1A in the **Supplementary Material**). In both RBC-free and RBC-laden flow scenarios, the flow distributions evolve from discrete high-/low-flow clusters towards a continuous exponential-like profile as the level of medium disorder increases, similar to earlier findings on Newtonian flows through perturbed cylinder arrays [11]. However, this evolution is noticeably accelerated in the presence of RBCs, *i.e.*, achieving an exponential-like flow distribution at lower level of disorder (Fig. 4B). Given that such exponential distribution is underpinned by less extreme local flow fractions at nodal points (*i.e.*, bifurcations) [11], the RBCs contribute to more robust perfusion of the porous domain, which is in line with a recent report on the role of RBCs in stabilising blood flow in the capillary bed [34]. Indeed, for strongly disordered geometry where flow channelisation (known to be associated with anomalous solute transport in heterogeneous media [35]) prevails in the plasma flow, the presence of RBCs is found to break down some dominant pathways and enhance regional perfusion (see Fig. S1B in the **Supplementary Material**).

Examination of the pore-scale dynamics reveals that the presence of RBCs introduces intermittent and/or permanent occlusion of narrow throats (Fig. 4A and **Supplementary Movie2**), featuring
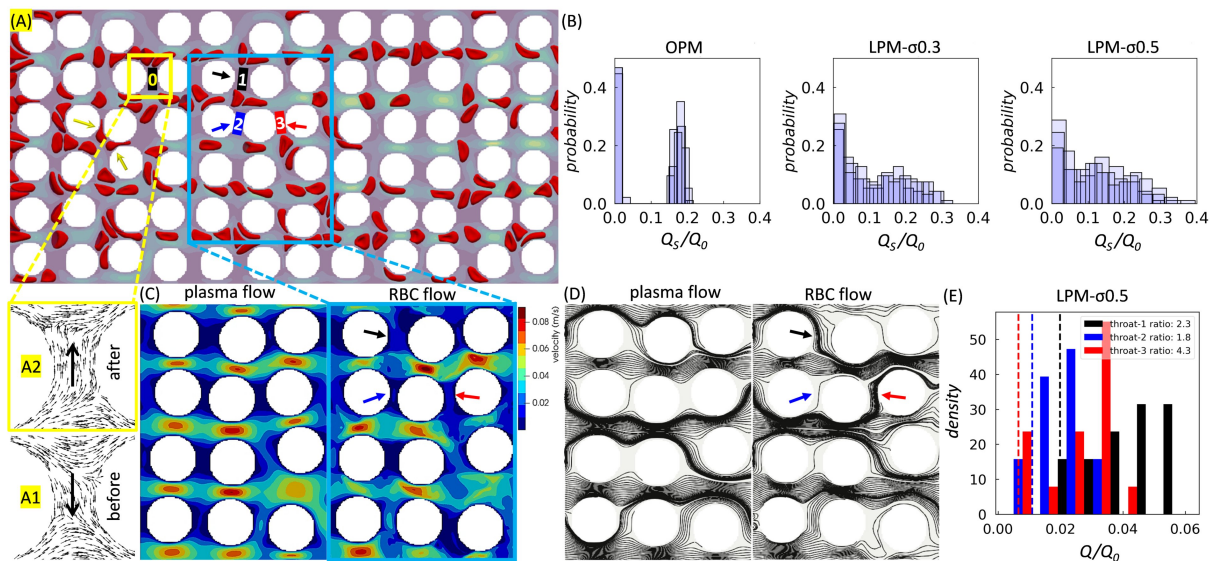
Figure 4: **Effect of RBC traffic on local flow patterns.** The porosity is $\phi = 0.57$, and the feeding haematocrit is $H_{\mathrm{F}} = 0.2$. Flow is from left to right. (A) Snapshot of an LPM simulation ($\sigma = 0.5$). The arrows (yellow) near the inlet indicate two cell-occlusion events. A small rectangle (yellow) marks a throat nearby ("0") within which flow reversal can be observed before (inset "A1") and after (inset "A2") the cell-occlusion events. Another rectangle (blue) marks the central region enlarged in (C,D) for pore-scale details. (B) Flow rate distributions for RBC flows through LPM with increasing levels of disorder $\sigma = 0$, 0.3, 0.5 (where $\sigma = 0$ refers to the OPM). The histograms show flow rate magnitudes Q_{s} evaluated at all throats within the pore space network, and $Q_0 = 0.4\,\mu\mathrm{L/min}$ is the imposed flow rate at the inlet. Three time instants are superimposed to show the temporal fluctuations due to the dynamics of discrete RBCs. (C) Instantaneous flow field (plasma-only and suspension) for the same $Q_0 = 0.4\,\mu\mathrm{L/min}$ ($\sigma = 0.5$). (D) Instantaneous streamlines for the same scenarios as in (C). The coloured arrows in (C,D) point to the three throats of interest ("1", "2", "3") marked in panel (A). (E) Quantification of the time-dependent RBC flow through the designated throats of interest as in (C,D). The histogram for each throat shows the probability of finding the instantaneous flow rate magnitude Q normalised by the imposed inflow Q_0; the histograms are obtained by evaluating fifteen time instants. The vertical dashed lines represent the corresponding steady and normalised plasma flow rates (magnitude) Q_{p}/Q_0 (note that the two lines for throats "1" and "3" have been moved away from each other by a finite distance for visual clarity, which would otherwise overlap). The ratios in the legend indicate the median suspension flow rate divided by the constant plasma flow rate in each throat investigated.

trapped RBCs between adjacent cylinders as observed in a recent experimental study [36]. Accompanied by such occlusion events are occasional flow reversals found in throats located in the vicinity (see Fig. 4A insets, "A1" and "A2"). These occlusions may in turn contribute to the diversion of flow (*via* occlusive pressure feedbacks [37]) to otherwise poorly infused regions (*e.g.*, vertically-oriented throats) and lead to more evenly distributed suspension flow in the system (see the enhanced transverse flows in Fig. 4C, right panel) compared with plasma-only flow (Fig. 4C, left panel) under identical inflow conditions. Indeed, the underlying streamline patterns in Fig. 4D suggest that some negligibly perfused throats in the plasma scenario become better perfused in the suspension scenario.

Furthermore, the RBCs impose a temporal signature on the pore-scale flow which is characterised by distinct patterns of flow channelisation over time (Fig. S2 in the **Supplementary Material**). To quantify
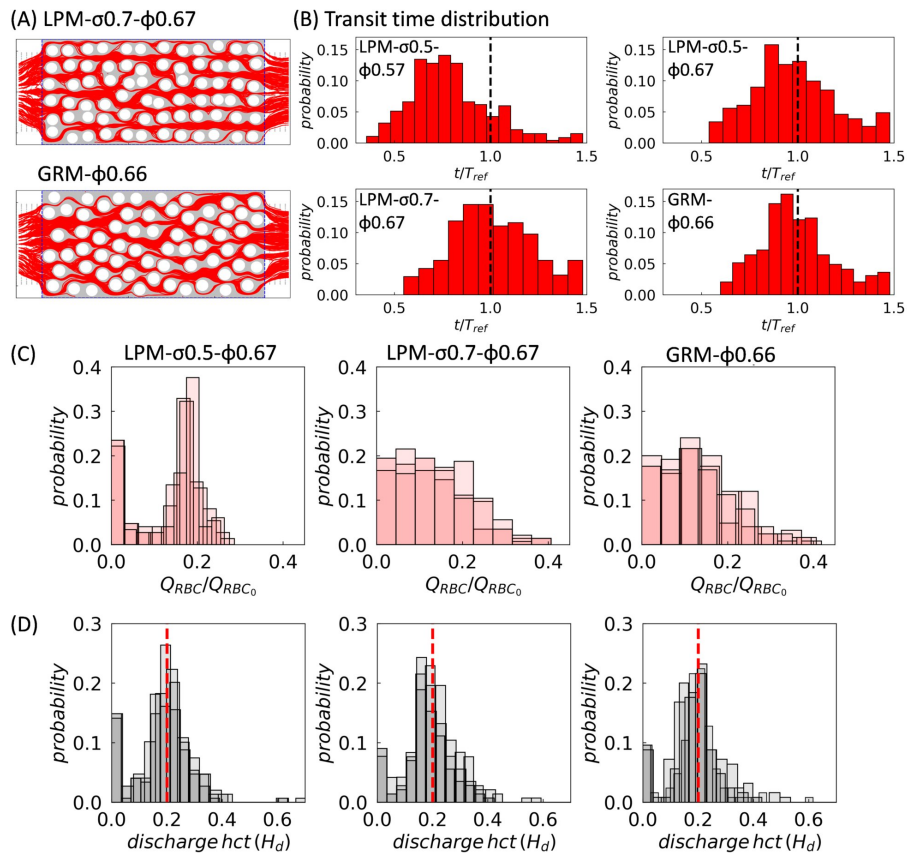
Figure 5: **Effect of disorder on RBC perfusion and haematocrit distribution.** (A) Combined RBC trajectories in simulation over a time period of 45 ms for LPM-σ0.7-ϕ0.67 and GRM-ϕ0.66. (B) Distributions of normalised RBC transit time subject to varying levels of porosity and disorder. The transit time is calculated based on each RBC entering and leaving the porous domain between the two vertical dashed lines (blue) in (A). The reference transit time T_{ref} was defined in Sec. 2.4. (C) RBC flux distributions corresponding to the high-porosity ($\phi = 0.66$–0.67) geometries in (B). The superimposed histograms from three consecutive time intervals for each geometry show the distribution of RBC fluxes evaluated at individual throats throughout the pore space network at three consecutive time intervals. (D) Distributions of discharge haematocrit H_{d} corresponding to the simulated RBC fluxes in (C).

the temporal variation, three throats of interest (Fig. 4E) are analysed for their instantaneous flow rates over fifteen time instants. Wide distributions of flow rates are found, and the time-averaged blood flow at the throats is roughly two to four times as high as in the plasma-only scenario. It is noteworthy that despite the highly dynamic RBC traffic and flow fluctuations at the pore scale, the pressure drop across the entire porous bed is essentially steady (see Fig. 3 for the narrow error bar ranges).

3.3 Increased disorder promotes homogeneous RBC transport and haematocrit distribution

RBC trajectories in the porous bed provide information about the spatiotemporal dynamics of the cells (compiled with over 1000 cells, Fig. 5A). Fig. 5B shows the corresponding distributions of RBC transit

times in geometries with different medium disorder. The data reveal that both the shape of the distribution and the median transit time are quantitatively similar in cases investigated here ($\phi = 0.67$), provided the porosity remains constant (confirmed for cases under $\phi = 0.57$ in Fig. S3A of the **Supplementary Material**). In other words, the transit time distributions are insensitive to the medium disorder under our studied range of porosity magnitudes. The insensitivity is likely caused by two opposing effects of structural disorder on the motion of RBCs: increasing the tortuosity of existing pathways slows down individual cell transits, but enables more flow pathways by creating local transverse pressure gradients. Our results suggest that, in a disordered porous medium such as the placental IVS [22], the average residence time of RBCs (associated with oxygenation and solute transport processes) within representative tissue volumes can be independent of the inherent structural heterogeneity if the tissue porosity remains roughly the same.

On the other hand, increasing the porosity from $\phi = 0.57$ to $\phi = 0.67$, while keeping the disorder unchanged, leads to an *increase* in median transit time (compare "LPM-σ0.5-ϕ0.57" and "LPM-σ0.5-ϕ0.67" in Fig. 5B). This seemingly counter-intuitive effect (*i.e.*, slower flow under relaxed confinement) is due to an overall smaller interstitial flow speed at higher porosity under the imposition of a *constant* feeding flow rate Q_0 (rather than constant pressure drop Δp). The evidently altered pattern of RBC transit times by a moderate change in the medium porosity suggests a potential mechanism for impaired placental function in pre-eclamptic or diabetic pathologies, where the porous tissues have been found either overly sparser or denser than under normal conditions [38].

Finally, we examine the spatiotemporal RBC distribution in more detail. A visual inspection of the time-lapse RBC perfusion reveals that there are still plenty of throats devoid of RBCs for the intermediate disorder $\sigma = 0.5$ (**Supplementary Movie4**); however, for higher degree of perturbed disorder $\sigma = 0.7$ and the random disorder (Figure 5A and **Supplementary Movie5–6**), the pore space network is more strongly perfused (also see). Fig. 5C shows the RBC flux distributions in the throats of the networks. These data confirm that the locally-perturbed "LPM-σ0.7" and the globally-random "GRM" have comparable RBC distributions while the less disordered "LPM-σ0.5" features a large number of throats without RBCs.

The discharge haematocrits H_d of individual throats tend to be close to the systemic haematocrit $H_F = 0.2$ as the structural disorder becomes sufficiently large in the system (*e.g.*, $\sigma \geq 0.5$), featuring a primary peak located around $H_d = H_F$ in the distribution profile (Fig. 5D). This concentrated distribution around $H_d = 0.2$ is still visible for weakly disordered geometries with $\sigma \leq 0.3$, but outweighed by a more dominant peak at zero (Fig. S3B in the **Supplementary Material**).

4   Conclusion

We have investigated the micro-haemodynamics of cellular blood flow in a class of porous media as a canonical model for extravascular geometries representative of biological tissues such as the porous intervillous space in the human placenta. Two types of canonical porous media with varying degrees of porosity were considered: weakly disordered porous media based on a regular square array of circular obstacles in a flat channel, and a random porous medium with non-overlapping circular obstacles. We employed simulations combining the lattice-Boltzmann, finite-element and immersed-boundary methods to explore the effects of haematocrit, porosity and structural disorder on the blood rheology, perfusion and distribution of red blood cells (RBCs) in the porous media. We used scaled-up experiments with droplets to validate the simulation framework. We found that the flux and velocity distribution of the simulated RBCs and measured droplets are qualitatively and quantitatively similar.

The findings from the simulations are threefold:

1. The relative apparent viscosity of cellular blood increases with the structural disorder of the porous media considered here, but it is largely independent of the studied porosity. These counter-intuitive

findings are likely caused by competing effects due to reduction of the cell-free layer thickness and cell ordering in narrow channels.

2. The presence of RBCs dynamically alters the flow distribution in the porous media investigated here. Throats that are only weakly perfused in the absence of RBCs can receive significantly higher flow due to RBCs partially blocking the flow in other, better-perfused throats. Due to the motion of the RBCs, the flow rates in the throats can fluctuate strongly.

3. Increasing the structural disorder of the porous media considered here promotes a more homogeneous distribution of RBCs as measured by cell fluxes and discharge haematocrits. While RBCs favour fast lanes through ordered or weakly disordered porous media, a stronger perturbation creates new pathways for the RBCs, leading to a more homogeneous haematocrit distribution throughout the geometry.

We have presented an experimental-computational framework for studying the micro-haemodynamics in disordered porous media. Our framework can be extended to more realistic architectures of biological tissues and organs. We envision that a multi-disciplinary approach, cross-validating simulations and experiments to extract generalised constitutive relationships for RBC flow in complex geometries, will help bridge the gap between microscopic characterisation and tissue/organ-level modelling which are both necessary to reveal the relationship between structure and function of biological tissue and organs.

5   Data accessibility

Data and information supporting this article are provided in the electronic supplementary materials. The source code for the blood flow simulations is available at `https://github.com/hemelb-codes/hemelb`.

6   Authors' contributions

Q.Z. designed the study, analysed the data and wrote the manuscript; Q.Z. (computational modelling), K.S., Q.C. and N.S. (microfluidic experiments), and E.D. (mathematical analysis) performed the research; P.R.S., M.O.B. and O.E.J. discussed the results and revised the manuscript; A.J., I.L.C. and T.K. supervised the study and edited the manuscript. All authors critically reviewed the manuscript and approved the final version for publication.

7   Competing interests

The authors declare that they have no competing interests.

8   Funding

11

9   Acknowledgements

References

[1] R. M. Padmos, T. I. Józsa, W. K. El-Bouri, P. R. Konduri, S. J. Payne, and A. G. Hoekstra, "Coupling one-dimensional arterial blood flow to three-dimensional tissue perfusion models for in silico trials of acute ischaemic stroke," *Interface Focus*, vol. 11, no. 1, p. 20190125, 2021.

[2] F. Schmid, G. Conti, P. Jenny, and B. Weber, "The severity of microstrokes depends on local vascular topology and baseline perfusion," *eLife*, vol. 10, p. e60208, 2021.

[3] F. Goirand, T. Le Borgne, and S. Lorthois, "Network-driven anomalous transport is a fundamental component of brain microvascular dysfunction," *Nature Communications*, vol. 12, no. 1, p. 7295, 2021.

[4] Q. Zhou, T. Perovic, I. Fechner, L. T. Edgar, P. R. Hoskins, H. Gerhardt, T. Krüger, and M. O. Bernabeu, "Association between erythrocyte dynamics and vessel remodelling in developmental vascular networks," *Journal of The Royal Society Interface*, vol. 18, no. 179, p. 20210113, 2021.

[5] S. Ebrahimi and P. Bagchi, "A computational study of red blood cell deformability effect on hemodynamic alteration in capillary vessel networks," *Scientific Reports*, vol. 12, no. 1, p. 4304, 2022.

[6] P. W. Sweeney, A. d'Esposito, S. Walker-Samuel, and R. J. Shipley, "Modelling the transport of fluid through heterogeneous, whole tumours in silico," *PLOS Computational Biology*, vol. 15, no. 6, p. e1006751, 2019.

[7] H. Li, Y. Deng, K. Sampani, S. Cai, Z. Li, J. K. Sun, and G. E. Karniadakis, "Computational investigation of blood cell transport in retinal microaneurysms," *PLOS Computational Biology*, vol. 18, no. 1, p. e1009728, 2022.

[8] O. E. Jensen and I. L. Chernyavsky, "Blood Flow and Transport in the Human Placenta," *Annual Review of Fluid Mechanics*, vol. 51, no. 1, pp. 25–47, 2019.

[9] A. R. Clark, T. C. Lee, and J. L. James, "Computational modeling of the interactions between the maternal and fetal circulations in human pregnancy," *WIREs Mechanisms of Disease*, vol. 13, no. 1, p. e1502, 2021.

[10] A. F. Morais, H. Seybold, H. J. Herrmann, and J. S. Andrade, "Non-Newtonian Fluid Flow through Three-Dimensional Disordered Porous Media," *Physical Review Letters*, vol. 103, no. 19, p. 194502, 2009.

[11] K. Alim, S. Parsa, D. A. Weitz, and M. P. Brenner, "Local Pore Size Correlations Determine Flow Distributions in Porous Media," *Physical Review Letters*, vol. 119, no. 14, p. 144501, 2017.

[12] H. J. Seybold, U. Eberhard, E. Secchi, R. L. C. Cisne, J. Jiménez-Martínez, R. F. S. Andrade, A. D. Araújo, M. Holzner, and J. Andrade, "Localization in Flow of Non-Newtonian Fluids Through Disordered Porous Media," *Frontiers in Physics*, vol. 9, p. 5, 2021.

[13] A. Puyguiraud, P. Gouze, and M. Dentz, "Pore-Scale Mixing and the Evolution of Hydrodynamic Dispersion in Porous Media," *Physical Review Letters*, vol. 126, no. 16, p. 164501, 2021.

[14] T. W. Secomb, "Blood Flow in the Microcirculation," *Annual Review of Fluid Mechanics*, vol. 49, no. 1, pp. 443–461, 2017.

[15] P. Balogh and P. Bagchi, "Direct Numerical Simulation of Cellular-Scale Blood Flow in 3D Microvascular Networks," *Biophysical Journal*, vol. 113, no. 12, pp. 2815–2826, 2017.

[16] G. Závodszky, B. van Rooij, V. Azizi, S. Alowayyed, and A. Hoekstra, "Hemocell: A high-performance microscopic cellular library," *Procedia Computer Science*, vol. 108, pp. 159–165, 2017.

[17] J. Ames, D. F. Puleri, P. Balogh, J. Gounley, E. W. Draeger, and A. Randles, "Multi-GPU immersed boundary method hemodynamics simulations," *Journal of Computational Science*, vol. 44, p. 101153, 2020.

[18] D. Alexeev, L. Amoudruz, S. Litvinov, and P. Koumoutsakos, "Mirheo: High-performance mesoscale simulations for microfluidics," *Computer Physics Communications*, vol. 254, p. 107298, 2020.

[19] A. L. Blumers, M. Yin, H. Nakajima, Y. Hasegawa, Z. Li, and G. E. Karniadakis, "Multiscale parareal algorithm for long-time mesoscopic simulations of microvascular blood flow in zebrafish," *Computational Mechanics*, vol. 68, no. 5, pp. 1131–1152, 2021.

[20] M. O. Bernabeu, J. Köry, J. A. Grogan, B. Markelc, A. Beardo, M. d'Avezac, R. Enjalbert, J. Kaeppler, N. Daly, J. Hetherington, T. Krüger, P. K. Maini, J. M. Pitt-Francis, R. J. Muschel, T. Alarcón, and H. M. Byrne, "Abnormal morphology biases hematocrit distribution in tumor vasculature and contributes to heterogeneity in tissue oxygenation," *Proceedings of the National Academy of Sciences*, vol. 117, no. 45, pp. 27811–27819, 2020.

[21] A. F. Smith, V. Doyeux, M. Berg, M. Peyrounette, M. Haft-Javaherian, A.-E. Larue, J. H. Slater, F. Lauwers, P. Blinder, P. Tsai, D. Kleinfeld, C. B. Schaffer, N. Nishimura, Y. Davit, and S. Lorthois, "Brain Capillary Networks Across Species: A few Simple Organizational Requirements Are Sufficient to Reproduce Both Structure and Function," *Frontiers in Physiology*, vol. 10, 2019.

[22] W. M. Tun, G. Poologasundarampillai, H. Bischof, G. Nye, O. N. F. King, M. Basham, Y. Tokudome, R. M. Lewis, E. D. Johnstone, P. Brownbill, M. Darrow, and I. L. Chernyavsky, "A massively multi-scale approach to characterizing tissue architecture by synchrotron micro-CT applied to the human placenta," *Journal of The Royal Society Interface*, vol. 18, no. 179, p. 20210140, 2021.

[23] Q. Zhou, E. Doman, K. Schirrmann, Q. Chen, E. A. Seed, E. D. Johnstone, P. R. Selvaganapathy, A. Juel, O. E. Jensen, M. O. Bernabeu, T. Krüger, and I. L. Chernyavsky, "Micro-haemodynamics at the maternal–fetal interface: Experimental, theoretical and clinical perspectives," *Current Opinion in Biomedical Engineering*, vol. 22, p. 100387, 2022.

[24] M. Dabaghi, N. Rochow, N. Saraei, G. Fusch, S. Monkman, K. Da, A. Shahin-Shamsabadi, J. L. Brash, D. Predescu, K. Delaney, C. Fusch, and P. R. Selvaganapathy, "A Pumpless Microfluidic Neonatal Lung Assist Device for Support of Preterm Neonates in Respiratory Distress," *Advanced Science*, vol. 7, no. 21, p. 2001860, 2020.

[25] J. T. Gostick, Z. A. Khan, T. G. Tranter, M. D. r Kok, M. Agnaou, M. Sadeghi, and R. Jervis, "PoreSpy: A Python Toolkit for Quantitative Analysis of Porous Media Images," *Journal of Open Source Software*, vol. 4, no. 37, p. 1296, 2019.

[26] T. Krüger, F. Varnik, and D. Raabe, "Efficient and accurate simulations of deformable particles immersed in a fluid using a combined immersed boundary lattice Boltzmann finite element method," *Computers & Mathematics with Applications*, vol. 61, no. 12, pp. 3485–3505, 2011.

[27] T. Krüger, *Computer Simulation Study of Collective Phenomena in Dense Suspensions of Red Blood Cells under Shear*. Vieweg+Teubner Verlag, 2012.

[28] Q. Zhou, J. Fidalgo, L. Calvi, M. O. Bernabeu, P. R. Hoskins, M. S. N. Oliveira, and T. Krüger, "Spatiotemporal Dynamics of Dilute Red Blood Cell Suspensions in Low-Inertia Microchannel Flow," *Biophysical Journal*, vol. 118, no. 10, pp. 2561–2573, 2020.

[29] K. Schirrmann, G. Cáceres-Aravena, and A. Juel, "Self-assembly of coated microdroplets at the sudden expansion of a microchannel," *Microfluidics and Nanofluidics*, vol. 25, no. 3, p. 29, 2021.

[30] J.-Y. Tinevez, N. Perry, J. Schindelin, G. M. Hoopes, G. D. Reynolds, E. Laplantine, S. Y. Bednarek, S. L. Shorte, and K. W. Eliceiri, "TrackMate: An open and extensible platform for single-particle tracking," *Methods*, vol. 115, pp. 80–90, 2017.

[31] A. R. Pries, D. Neuhaus, and P. Gaehtgens, "Blood viscosity in tube flow: Dependence on diameter and hematocrit," *American Journal of Physiology - Heart and Circulatory Physiology*, vol. 263, no. 6, pp. H1770–H1778, 1992.

[32] H. Stauber, D. Waisman, N. Korin, and J. Sznitman, "Red blood cell (RBC) suspensions in confined microflows: Pressure-flow relationship," *Medical Engineering and Physics*, vol. 48, pp. 49–54, 2017.

[33] S. Li, H.-h. Yu, and J. Fan, "Modeling transport of soft particles in porous media," *Physical Review E*, vol. 104, no. 2, p. 025112, 2021.

[34] F. Schmid, M. J. P. Barrett, D. Obrist, B. Weber, and P. Jenny, "Red blood cells stabilize flow in brain microvascular networks," *PLOS Computational Biology*, vol. 15, no. 8, p. e1007231, 2019.

[35] C. Bruderer-Weng, P. Cowie, Y. Bernabé, and I. Main, "Relating flow channelling to tracer dispersion in heterogeneous networks," *Advances in Water Resources*, vol. 27, no. 8, pp. 843–855, 2004.

[36] H. Stauber, D. Waisman, N. Korin, and J. Sznitman, "Red blood cell dynamics in biomimetic microfluidic networks of pulmonary alveolar capillaries," *Biomicrofluidics*, vol. 11, no. 1, p. 014103, 2017.

[37] S.-S. Chang, S. Tu, K. I. Baek, A. Pietersen, Y.-H. Liu, V. M. Savage, S.-P. L. Hwang, T. K. Hsiai, and M. Roper, "Optimal occlusion uniformly partitions red blood cells fluxes within a microvascular network," *PLOS Computational Biology*, vol. 13, no. 12, p. e1005892, 2017.

[38] A. S. Serov, C. M. Salafia, P. Brownbill, D. S. Grebenkov, and M. Filoche, "Optimal villi density for maximal oxygen uptake in the human placenta," *Journal of Theoretical Biology*, vol. 364, pp. 383–396, 2015.

[39] M. D. Mazzeo and P. V. Coveney, "HemeLB: A high performance parallel lattice-Boltzmann code for large scale fluid flow in complex geometries," *Computer Physics Communications*, vol. 178, no. 12, pp. 894–914, 2008.

[40] Y. H. Qian, D. D'Humières, and P. Lallemand, "Lattice BGK Models for Navier-Stokes Equation," *EPL (Europhysics Letters)*, vol. 17, no. 6, p. 479, 1992.

[41] P. L. Bhatnagar, E. P. Gross, and M. Krook, "A Model for Collision Processes in Gases. I. Small Amplitude Processes in Charged and Neutral One-Component Systems," *Physical Review*, vol. 94, no. 3, pp. 511–525, 1954.

[42] Z. Guo, C. Zheng, and B. Shi, "Discrete lattice effects on the forcing term in the lattice Boltzmann method," *Physical Review E*, vol. 65, no. 4, p. 046308, 2002.

[43] M. Bouzidi, M. Firdaouss, and P. Lallemand, "Momentum transfer of a Boltzmann-lattice fluid with boundaries," *Physics of Fluids*, vol. 13, no. 11, pp. 3452–3459, 2001.

[44] A. J. C. Ladd, "Numerical simulations of particulate suspensions via a discretized Boltzmann equation. Part 1. Theoretical foundation," *Journal of Fluid Mechanics*, vol. 271, pp. 285–309, 1994.

[45] M. O. Bernabeu, M. L. Jones, J. H. Nielsen, T. Krüger, R. W. Nash, D. Groen, S. Schmieschek, J. Hetherington, H. Gerhardt, C. A. Franco, and P. V. Coveney, "Computer simulations reveal complex distribution of haemodynamic forces in a mouse retina model of angiogenesis," *Journal of The Royal Society Interface*, vol. 11, no. 99, p. 20140543, 2014.

[46] C. S. Peskin, "The immersed boundary method," *Acta Numerica*, vol. 11, pp. 479–517, 2002.

Supplementary Materials

S1 Numerical model for cellular flow simulation

The immersed-boundary-lattice-Boltzmann method (IB-LBM [27]) is employed to simulate cellular blood flow as a suspension of deformable RBCs. The numerical model is implemented in the parallel flow simulator $HemeLB$ [39] (open source at https://github.com/hemelb-codes/hemelb), which has been successfully applied to cellular simulation in complex and sparse geometries (*e.g.*, realistic microvasculature [4]). The 3D fluid flow governed by the Navier-Stokes equations is solved by the lattice-Boltzmann method (LBM) with standard D3Q19 lattice [40], BGK collision operator [41], Guo's forcing scheme [42] and the Bouzidi-Firdaouss-Lallemand (BFL) implementation of no-slip condition at the walls [43]. Open boundary conditions for flow inlets/outlets are implemented with the Ladd velocity boundary condition [44]. To configure the simulation, each porous medium geometry (generated in STL format) is discretised into a uniform mesh of cubic voxels. The voxel size (*i.e.*, the lattice constant Δx) is chosen such that the plasma flow can be reliably solved at the narrowest pore-throats in the simulated porous media. The relaxation time parameter τ_{BGK} is determined based on a previous study [45] for minimising relative error of simulated flow rates. Refer to Table S1 for values of key simulation parameters.

The discrete RBCs are modelled as triangulated Lagrangian membranes using the finite element method (FEM) and are coupled with the fluid flow using the immersed-boundary method (IBM [46]). Each RBC consists of N triangular facets and present a discocyte shape at rest. The mesh resolution of the membrane is chosen such that the average edge length of the facets matches the voxel size Δx of the flow domain for numerical stability and accuracy [26]. The membrane is hyperelastic, isotropic and homogeneous, with its mechanical properties controlled by (κ_{s}, κ_{b}, κ_{α}, κ_{A}, κ_{V}) as mentioned in the main text. κ_{cc} and κ_{cw} are intensities of the repulsive potential (decaying with inverse distance) between neighbouring cells, and neighbouring cell-wall, respectively. The cytosol enclosed by the RBC membrane is regarded as a Newtonian fluid with same viscosity to the plasma. The membrane viscosity is not considered in the present material model. Refer to Table S1 for values of the above parameters.

Table S1: **Key parameters of the flow and RBC model.** "$\sim$" means dimensionless simulation units.

Parameter	Description	Value	Unit	Comment
Δx	lattice constant	0.4	μm	decided by minimal throat widths
Δt	time step length	1.6×10^{-8}	s	based on diffusive scaling
τ_{BGK}	relaxation time	0.8	–	minimising flow rate error
η_0	plasma viscosity	1	mPa s	same as liquid water
η_{cytosol}	cytosol viscosity	1	mPa s	assuming $\eta_{\mathrm{cytosol}} = \eta_0$
R_{rbc}	RBC radius	4	μm	present RBC model
T_{rbc}	RBC thickness	2.5	μm	present RBC model
A_{rbc}	RBC surface area	140	μm^2	present RBC model
V_{rbc}	RBC volume	100	μm^3	present RBC model
N	number of facets	2000	–	$N = 20(r_{\mathrm{rbc}}/\Delta x)^2$
Γ	Föppl-von Kármán number	400	–	$\Gamma = \kappa_{\mathrm{s}} r_{\mathrm{rbc}}^2 / \kappa_{\mathrm{b}}$
$\tilde{\kappa}_{\mathrm{s}}$	strain modulus	1.67×10^{-3}	–	resisting in-plane shearing
$\tilde{\kappa}_{\mathrm{b}}$	bending modulus	4.18×10^{-4}	–	resisting off-plane bending
$\tilde{\kappa}_{\alpha}$	dilation modulus	0.5	–	conserving local area
$\tilde{\kappa}_{\mathrm{A}}$	surface modulus	1	–	conserving cell surface
$\tilde{\kappa}_{\mathrm{V}}$	volume modulus	1	–	conserving cell volume
$\tilde{\kappa}_{\mathrm{cc}}$	repulsion intensity	$\tilde{\kappa}_{\mathrm{b}}$	–	cell-cell interaction
$\tilde{\kappa}_{\mathrm{cw}}$	repulsion intensity	$10\tilde{\kappa}_{\mathrm{b}}$	–	cell-wall interaction

S2   Empirical model for blood viscosity in tube flow

Capitalising on various sources of experimental data collected from literature, Pries and co-workers [31] derived an empirical model that depicts the variation of the apparent viscosity of blood η_{app} (relative to that of plasma η_0) in cylindrical tubes against the tube diameter D (formulated in μm) and discharge haematocrit H_{D}:

$$\eta_{\mathrm{rel}} = \frac{\eta_{\mathrm{app}}}{\eta_0} = 1 + (\eta_{45} - 1)\frac{(1 - H_{\mathrm{D}})^C - 1}{(1 - 0.45)^C - 1} \tag{S1}$$

where η_{45} is the relative apparent viscosity of blood at a discharge haematocrit $H_{\mathrm{D}} = 0.45$ formulated as

$$\eta_{45} = 220e^{-1.3D} + 3.2 - 2.44e^{-0.06D^{0.645}}, \tag{S2}$$

and C is a coefficient related to D in the form of

$$C = \left(0.8 + e^{-0.075D}\right)\left(-1 + \frac{1}{1 + 10^{-11}D^{12}}\right) + \frac{1}{1 + 10^{-11}D^{12}}. \tag{S3}$$

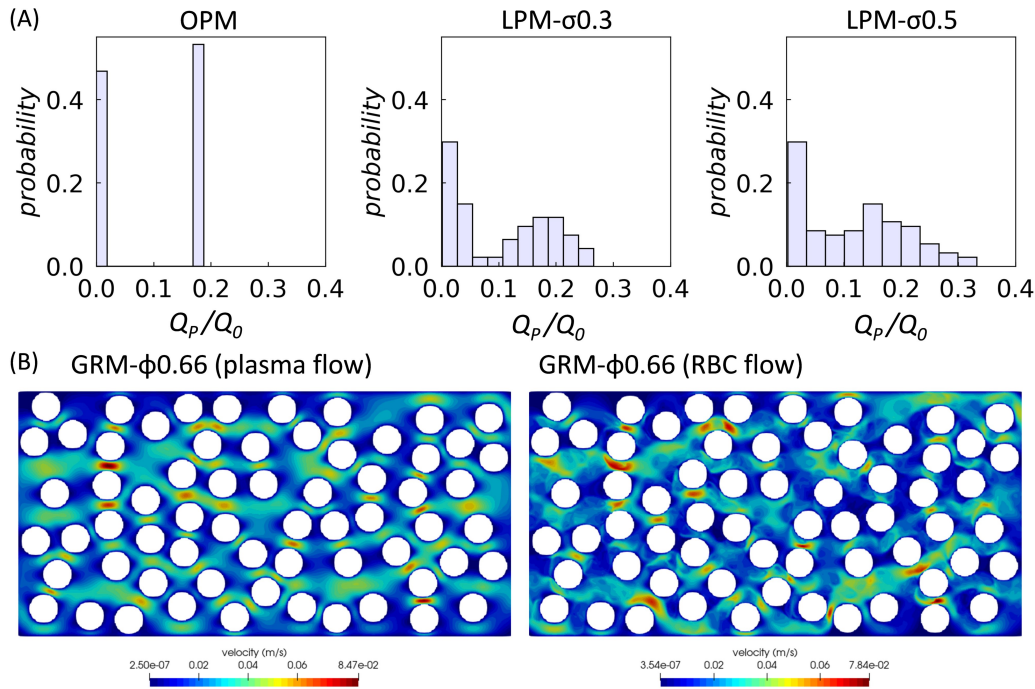## S3   Spatiotemporal dynamics of the RBC suspension flow

Figure S1: **Effect of RBCs interacting with structural disorder on flow distribution within the porous media.** (A) Flow rate distributions for steady plasma flows through LPM with increasing levels of disorder $\sigma = 0, 0.3, 0.5$ (where $\sigma = 0$ refers to the ordered porous medium), corresponding to the RBC flows Q_{s} ($H_{\mathrm{F}} = 20\%$) in Fig. 4B. Porosity is $\phi = 0.57$ in all cases. The histograms show flow rates Q_{p} evaluated at all throats within the pore space network. $Q_0 = 0.4\,\mu$L/min is the imposed flow rate at the inlet. (B) Flow channelisation patterns for (left) steady plasma flow and (right) RBC flow ($H_{\mathrm{F}} = 20\%$) in GRM-ϕ0.66 under the same inflow $Q_0 = 0.4\,\mu$L/min.
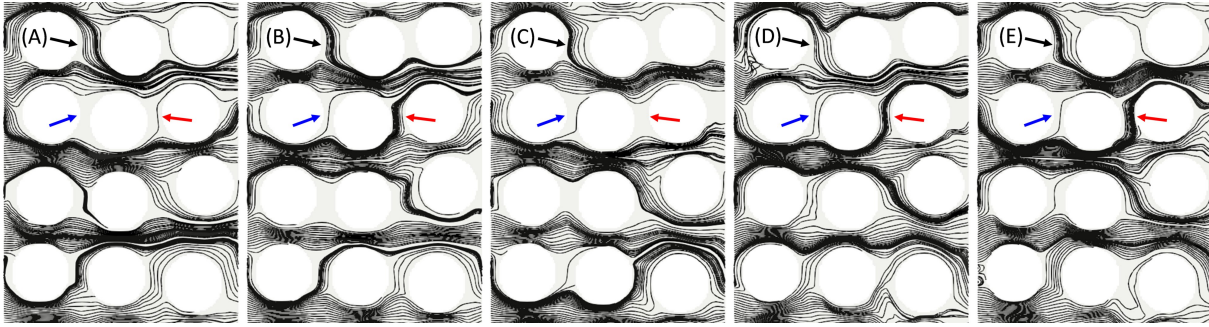
Figure S2:   **Instantaneous streamlines of the simulation in Fig. 4A.** The corresponding time instants are $t = 134.8$ ms, $t = 137.8$ ms, $t = 140.8$ ms, $t = 143.7$ ms, $t = 146.7$ ms, respectively. The temporal variation of the streamlines is caused by the dynamics of the discrete RBCs. The coloured arrows in (A–E) indicate the three throats of interest ("1", "2", "3") marked in panel Fig. 4A.

S4   Effect of medium porosity and disorder on RBC transport
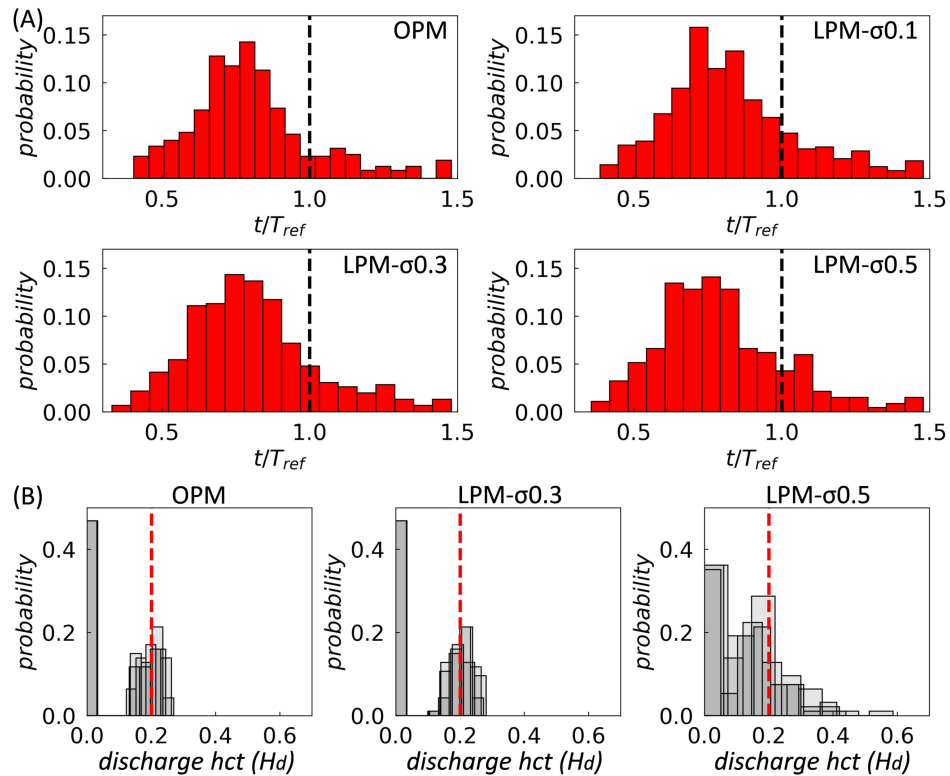

Figure S3:   Quantification of particle transit time and discharge haematocrit in other geometries ($\phi = 0.57$). (A) Transit time distributions in the OPM and LPM geometries ($\sigma = 0.1, 0.3, 0.5$). (B) Discharge haematocrit distributions in the OPM and weakly disordered LPM geometries ($\sigma = 0.1, 0.3$).

S5   Supplementary movies

Movie1   Video clip of the RBC simulation in OPM-ϕ0.57 ($H_{\mathrm{F}} = 0.2$).

Movie2   Video clip of the RBC simulation in LPM-σ0.5-ϕ0.57 ($H_{\mathrm{F}} = 0.2$).

Movie3   Video clip of the droplet experiment in LPM-σ0.5-ϕ0.57 ($H_{\mathrm{F}} = 0.2$).

Movie4   Video clip of the RBC simulation in LPM-σ0.5-ϕ0.67 ($H_{\mathrm{F}} = 0.2$).

Movie5   Video clip of the RBC simulation in LPM-σ0.7-ϕ0.67 ($H_{\mathrm{F}} = 0.2$).

Movie6   Video clip of the RBC simulation in GRM-ϕ0.66 ($H_{\mathrm{F}} = 0.2$).